Lab on a Chip

PAPER

View Article Online
View Journal | View Issue

Cite this: *Lab Chip*, 2025, **25**, 4436

Integrated heating & sensing for PCB EWOD chips on a digital microfluidics cloud platform†

Mosfera A. Chowdury,[a] Gnanesh Nagesh,[a] Eric Hyunsung Cho,[b] Qining Leo Wang,[b] Bhawya,[a] Abdulrahman Altabbaa,[a] Lina Rose,[ac] Simon Rondeau-Gagné,[c] Chang-Jin "CJ" Kim *[bde] and Mohammed Jalal Ahamed *[a]

Received 22nd May 2025,
Accepted 30th June 2025

DOI: 10.1039/d5lc00507h

rsc.li/loc

Digital microfluidics (DMF) based on electrowetting-on-dielectric (EWOD) is a versatile platform that offers automated and precise droplet handling. Despite advances, one of the critical components—an integrated thermal module—remains underdeveloped, limiting the accuracy and reliability of bioassays. This paper presents a new thermal management module compatible with printed circuit board (PCB)-based DMF devices co-fabricated through standard PCB manufacturing. It integrates a microheater and sensor pair interfaced with a closed-loop control system for individual droplet's temperature control. Numerical simulations were performed to understand heat transfer from the embedded microheaters to the droplets for optimized microheater design. Experiments were performed to evaluate key performance metrics of the module, including temperature accuracy, control stability, response time, crosstalk, and heat localization. Finally, a glucose assay was conducted on-chip to demonstrate the module's applicability. The co-fabricatable heating-sensing module design presented in this paper offers seamless integration of thermal management for PCB-based DMF chips at little additional manufacturing cost while supporting the cloud-based platform established to democratize DMF.

Introduction

Digital microfluidics (DMF)[1,2] is a technology that independently manipulates fluid droplets in picoliters to microliters. Unlike continuous-flow microfluidics, which require pumps, valves, and channels, DMF programmatically controls individual droplets on a surface, most commonly by using electrowetting-on-dielectric (EWOD) actuation.[3–7] By leveraging and combining the four basic EWOD microfluidic operations—creating, transporting, cutting, and merging of droplets[5]—numerous diverse and complex biological and chemical protocols have been developed over the years to automate the liquid handling process on DMF chips.[8–17]

Regardless of the application type, fully automating wet laboratory-based biological or chemical protocols often requires precise temperature control to enable specific biochemical reactions.[18–20] To implement such tests on DMF systems, effective and localized temperature regulation is crucial. Therefore, a wide range of temperature control approaches, involving microheaters, heating elements, temperature sensors, and microcontrollers, have been adopted for the thermal regulation on DMF chips. Some groups have integrated heaters and sensors into the DMF chip by patterning them along with the EWOD electrodes.[21,22] Others have attached heaters and sensors to the DMF chip by patterning them on the other side of the substrate plate or the cover plate before assembling the two.[19,23,24] More commonly, many laboratories have utilized discrete heaters and temperature sensors by placing them against the DMF chip at the system level.[25–30] All these approaches materialize bioassays on chips for unique applications, and some of these concepts have advanced into benchtop DMF platforms.

Benchtop DMF platforms with external system-level subcomponents—such as control systems, software, thermal control, and DMF chips—have been developed in both academic and industrial settings. Notable examples include from Baebies,[31] OpenDrop,[32] DropBot,[33] PurpleDrop,[34] LampPort,[35] PhageBox,[36] PortaDrop,[37] and aQdrop.[38] Some of the above platforms are glass-based chips whereas others are printed circuit board (PCB)-

[a] *Mechanical, Automotive and Materials Engineering, University Windsor, Windsor, ON, N9B 3P4, Canada. E-mail: jahamed@uwindsor.ca*
[b] *Mechanical and Aerospace Engineering Department, University of California, Los Angeles (UCLA), Los Angeles, California 90095, USA. E-mail: cjkim@ucla.edu*
[c] *Chemistry and Biochemistry, University Windsor, Windsor, ON, N9B 3P4, Canada*
[d] *Bioengineering Department, University of California, Los Angeles (UCLA), Los Angeles, California 90095, USA*
[e] *California NanoSystems Institute (CNSI), University of California, Los Angeles (UCLA), Los Angeles, California 90095, USA*

† Electronic supplementary information (ESI) available. See DOI: https://doi.org/10.1039/d5lc00507h

based EWOD DMF chips[39,40] which are used by most commercial products today[41] and are the main interest in this research. These platforms often use generic thermal controllers, such as Peltier chips, thermal blocks, and thin-film heaters. Since they are discrete components, additional manufacturing and packaging steps are needed for interfacing to complete the system and may increase the complexity and cost of the final product. Larger resistive elements or external heating elements also present challenges, such as slow temperature transitions and large thermal inertia due to the thermal mass of the extended layer or component.[42,43] These issues can complicate precise thermal control, especially when the thermal profile involves multiple temperature transitions. To avoid the use of bulky heating modules and ensure accurate localized heating,[40] efforts have been made to develop PCB-based DMF chips integrated with temperature control. For example, Wu *et al.*[44] used screen-printed carbon black heaters atop the PCB layer. The additional manufacturing step of screen printing can be avoided if one integrates the heaters inside the copper layers of the PCB. For example, Tanev *et al.*[45] reported a modular platform, BiowareCFP, where a microheater was integrated inside the PCB, looping around the vias. Although this concept is useful for generating heat, the platform requires integrated sensing to avoid possible uneven heating and is incapable of consistently generating localized heating, which is essential for conducting a PCR thermal-modulated cycle.[45] The PCB EWOD chips integrated with thermal systems for a benchtop DMF platform, whether using the copper layer as a heater or a sensor yet lacks integrated heating or sensing mechanisms without the need for an external heater or sensor. Additionally, no reliable implementation of sensing and closed-loop actuation application of the integrated microheater was demonstrated. Similarly, it is unclear whether the heater module can reliably shift between different temperature zones, which is critical for performing certain bioassays. In addition to DMF, integrated heater layers inside a multilayer PCB have shown that the system can achieve a uniform temperature on the top conductive layer.[46] To overcome the thermal variability at the top conductive layer, vertical and horizontal microheaters were sandwiched between two conductive layers of the PCB.[46] A similar approach could be beneficial for multilayer PCB-based EWOD DMF chips. However, such designs need to incorporate sensor layers, EWOD electrodes and electrical access to them as well as robust integrated sensing and control to maintain a uniform temperature across the chip surface.

Although portable platforms for performing DMF-based assays exist, the above discussion highlights the challenges and gaps in developing a robust integrated thermal module that can provide real-time temperature feedback control with minimal power consumption. Additionally, to make the results useful for a wide range of users, we are compelled to develop integrated thermal control for a PCB EWOD chip on a DMF platform designed with a standardized and user-friendly technology infrastructure. Previously, Wang *et al.* reported *eDroplets*, a cloud-based DMF platform that provides users with an open ecosystem that provides essential, standardized infrastructure for developing DMF-based products and applications.[47,48] While advancing integrated thermal control for PCB DMF chips, this work further aims to develop a microheater–sensor pair integrated into a PCB DMF chip compatible with *eDroplets*. With the ability to regulate precise thermal management at the chip level, the portable DMF system demonstrates that a PCB-based chip-level thermal control module can regulate temperatures while running a biochemical reaction on a chip. Owing to its simple and adaptable design, the proposed integrated thermal control is promising as an effective heater module to complete the portable DMF system for bioassays.

The remainder of this paper briefly describes the hardware design of the *eDroplets* platform on the basis of a previously published article.[48] Then we outline the micro heater-sensor design and numerical simulation of heat transfer between the heater-integrated PCB and a droplet on it, controller development, experimentation, and demonstration of a glucose assay to assess the performance of the integrated DMF chip with heater-sensor pair operating on the *eDroplets* platform.

Materials & methods

Materials

The glucose assay used in this study was composed of copper(II) sulphate pentahydrate ($CuSO_4{\cdot}5H_2O$), a glucose solution ($C_6H_{12}O_6$) (Thermo Fisher Scientific Canada), sodium hydroxide (NaOH), and potassium sodium tartrate tetrahydrate ($C_4H_4KNaO_6{\cdot}4H_2O$) (Millipore Sigma Canada).

The design tools used for circuit and layout development are Altium Designer (version 24.0.1) and KiCad (version 7). Heater controller performance analysis was performed *via* the Keysight U5855A TrueIR Thermal Imager (Santa Rosa, CA, USA). The analysis and numerical tools used were Keysight TrueIR analysis and COMSOL Multiphysics Version 6.2.

Cloud-based DMF platform – eDroplets

The thermal management technology in this paper was developed to be an added functionality for PCB-based DMF devices designed and operated on a cloud-based DMF platform,[47] currently named *eDroplets* (**https://www.edroplets.org/**). The platform guides the user in designing, fabricating, and operating their own EWOD DMF chip by offering an EWOD CAD and a DMF chip. The graphical user interface (GUI)-based CAD helps the user's layout their own EWOD chip while enforcing design rules that ensure successful fabrication. The DMF control system allows quick and easy insertion and operation of the EWOD chip using a GUI-based actuation tool. The added technology enables users to integrate a microheater and a temperature sensor immediately below selected EWOD electrodes, allowing droplets to shuttle to temperature-controlled spots and accommodating a wide range of biochemical analyses. To test its utility, a new PCB DMF chip was designed, and a reliable and sensitive thermal biochemical process was performed on the custom chip using the portable DMF control system.

Hardware design

The overall design of our integrated heating-sensing system for cloud-based digital microfluidics is shown in Fig. 1. Fig. 1(a) shows a cross-sectional view of the EWOD PCB layers covered with a polypropylene plastic top plate and the droplets between them. Fig. 1(b) shows the top view of the EWOD electrodes present in the PCB's top copper layer. Fig. 1(c) shows the serpentine-shaped microheater we employed, which is present in the second copper layer of the PCB. The *eDroplets* platform involves two main hardware parts: an EWOD DMF chip and a DMF control system, as shown in Fig. 1(d). As detailed in Wang *et al.*,[47] the control system consists of four key components: an aluminum chassis, electronic circuits, a chip-system interface, and a web-based GUI. The chip-system interface consists of pogo pins for reliable electrical contacts and an alignment stencil for easy placement of the EWOD chip. The web-based GUI facilitates customizable droplet actuation sequences and debugging capabilities. Leveraging the *eDroplets* platform, heating and sensing elements have been integrated into and co-fabricated with an EWOD chip, resulting in a DMF chip with a thermal management capability. A heating and sensing circuit are directly connected with the integrated microheater and sensor in the PCB such that the microheater can heat a specific droplet on the EWOD surface and the sensor can sense the temperature of the top surface. To operate these microheaters and sensors, specific controllers have been configured, as detailed in the following section.

Microheater & sensor design

To optimize the thermal response of the EWOD surface heated by an integrated heater and estimate the temperature distribution inside the liquid droplet surrounded by a filler fluid medium, such as air or silicone oil, a finite element simulation model was developed in COMSOL Multiphysics. The simulation is critical for understanding the thermal response during design to achieve the desired thermal response. Two widely used heater designs were utilized to evaluate the overall performance: a serpentine-shaped heater and a double spiral-shaped heater. The design schematics and thermal simulations for both configurations are presented in Fig. S1(a) and (b),† respectively.

The design of the sensor mirrors that of the microheater to maintain consistency and compatibility between different DMF chips. As the PCB has multiple copper layers, one layer is used as the microheater, and the other layer is used as the sensor layer. Consequently, the following two sections focus on the design and working principle of the heater, including its operation and heat transfer from the integrated microheater to the aqueous droplet.

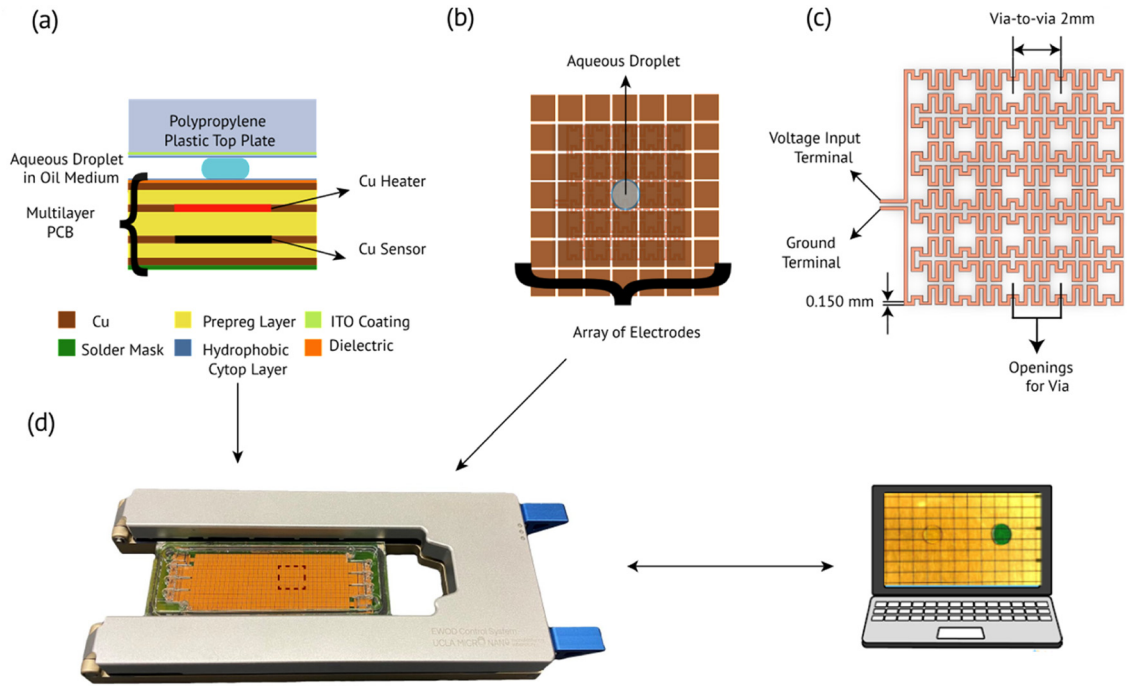

Fig. 1 Overview of our modular EWOD DMF system with integrated heater-sensor showing (a) a cross-section view of the *eDroplets* PCB EWOD device developed for this study, consisting of aqueous droplet between a top plate and a PCB. Structural layers of the EWOD PCB showing that below the first copper layer of EWOD electrodes, serpentine-shaped microheaters and sensors are embedded in the second and third copper layers, respectively. (b) A top view of the *eDroplets* PCB EWOD device, showing an aqueous droplet over patterns of EWOD electrodes, heater, and sensor (not drawn to scale). (c) The heater and sensor serpentine lines are 150 μm wide and designed to cover a 5 × 5 array of EWOD electrodes, each measuring around 2 mm × 2 mm and maintaining a 2 mm *via*-to-*via* pitch. (d) The testing setup consists of an *eDroplets* PCB EWOD device is installed in the *eDroplets* DMF modular control system. Users run experiments using a web-based DMF control graphical user interface (GUI) (**https://gui.edroplets.org/**) *via* a PC connected to the control system.

To achieve localized heating beneath a specific droplet of interest, the heater and sensor were designed to cover a 5 × 5 array of EWOD electrodes, corresponding to an area of 10 mm × 10 mm. To increase the platform's versatility, three identical microheaters and sensors were integrated into a 20.0 cm × 8.2 cm DMF chip designed on the *eDroplets* platform. The gap height between the top polypropylene plastic top plate and the PCB is 150 μm (Fig. 1(a)). A droplet positioned within the 150 μm gap between the top plate and the EWOD surface was modeled to analyze the thermal behavior.

Working principle & governing equations for heating simulation

A microheater generally operates on the basis of the Joule heating effect. To understand the heater's ability to heat the top surface, a COMSOL Multiphysics simulation was performed on a resistive copper heater, as shown in Fig. S2.† The following governing equation for heat conduction through solids was solved numerically:

$$\rho C_p u \cdot \nabla T + \nabla q = Q \quad (1)$$

Here, C_p and Q denote the specific heat and heat sink, respectively.

Afterwards the COMSOL Multiphysics simulation was subsequently extended to understand the heat transfer between the solid layers and the transfer of thermal energy to the droplet with the application of an actuation voltage to the copper layer heater inside the device. The final COMSOL simulation Multiphysics model also included the heat transfer in solids and fluids interface and was configured to account for both convection and conduction. For the numerical simulation, the heat capacity values for both the copper layer and FR4 glass epoxy were 384 J kg^{-1} K^{-1} and 1369 J kg^{-1} K^{-1}, respectively, and the thermal conductivities were 401 W m^{-1} K^{-1} and 0.3 W m^{-1} K^{-1}, respectively. Widely used serpentine and double-spiral heaters were compared for different applied actuation voltages in the simulation. The heating capabilities of both microheater designs were similar for the temperature range of 40 °C to 120 °C (Fig. S3a and b†). Both Fig. S3(a) and (b)† show that regardless of the design, both microheaters can heat the top EWOD electrode copper surface to the target temperature when the required voltage is applied. Furthermore, this numerical simulation result shows that despite having different geometric shapes, both microheaters perform similarly. We have included the convective heat flux physics to solve for the convection inside the droplet in simulation during heat transfer.

We hypothesized that the thickness of the heater layer can impact on the heating capacity as the resistance changes. The impact of the thickness and input voltage requirement to achieve the target temperature is investigated and shown in Fig. S4(a–c),† demonstrating that for a thinner layer, a higher voltage is required to achieve the same temperature.

To further investigate the heat transfer from the PCB layer to the droplet, an aqueous droplet surrounded by filler fluid, *i.e.*, silicone oil, was simulated. The numerical simulation results, shown in Fig. 2(a) and (b), indicate the heatmap of the top EWOD surface in the presence of an applied voltage. The results shown in Fig. 2(c) and (d) indicate that the heat generated by the microheater is sufficient to heat the liquid droplet in a filler fluid. The observations of the numerical simulation are explained in more detail in the 'Results and discussion' section.

Microheater & sensor system

A microcontroller-based heater controller, actuation, and sense circuit were designed to understand the performance of the serpentine microheater. The hardware consisted of an Arduino Uno board, a transistor, a voltage regulator, and a 5 V power supply. The majority of the circuits were subdivided into heating circuits and sense circuits. The heating circuit was responsible for controlling the heater, and the sensor circuit measured the temperature *via* changes in the resistance (Fig. S5(a)†). The closed-loop controller with a proportional integrator derivative (PID) and pulse width modulation (PWM) is shown in Fig. S5(b).† The open-loop and feedback control system circuits are shown in Fig. S5(a).†

Sense circuit development & signal amplification

The sense circuit employs a sensor with a design identical to that of the microheater and is positioned on the copper layer directly beneath the heater. The quantitative value across the sensing resistor was measured as a proportional value to the sensor's resistor, providing an indirect measurement of the surface temperature. For this, the sensing resistor placed in a Wheatstone bridge configuration. The drop in voltage at Wheatstone is due to the change in resistance fed into the analog input pin of the microcontroller, which provided a signal that reflected the temperature of the surface.

Although the resistance change was measurable, the difference was typically in the milli-ohm range, which was low, making detection challenging for the microcontroller. To address this limitation, a bridge configuration together with a general-purpose operational amplifier (op-amp) was employed to amplify the voltage difference across the sensing resistor (Fig. 3(a)). The sensor was calibrated to sense the top surface temperature by placing a thermocouple on the top surface, and the calibration curve is shown in Fig. 3(b).

Heating circuit development

The core component of the heater circuit was an NPN transistor (TIP120), configured with its collector connected to a 5 V supply, its emitter linked to the heater, and its base driven by the pulse width modulation (PWM) pin of a microcontroller. By adjusting the duty cycle of the PWM

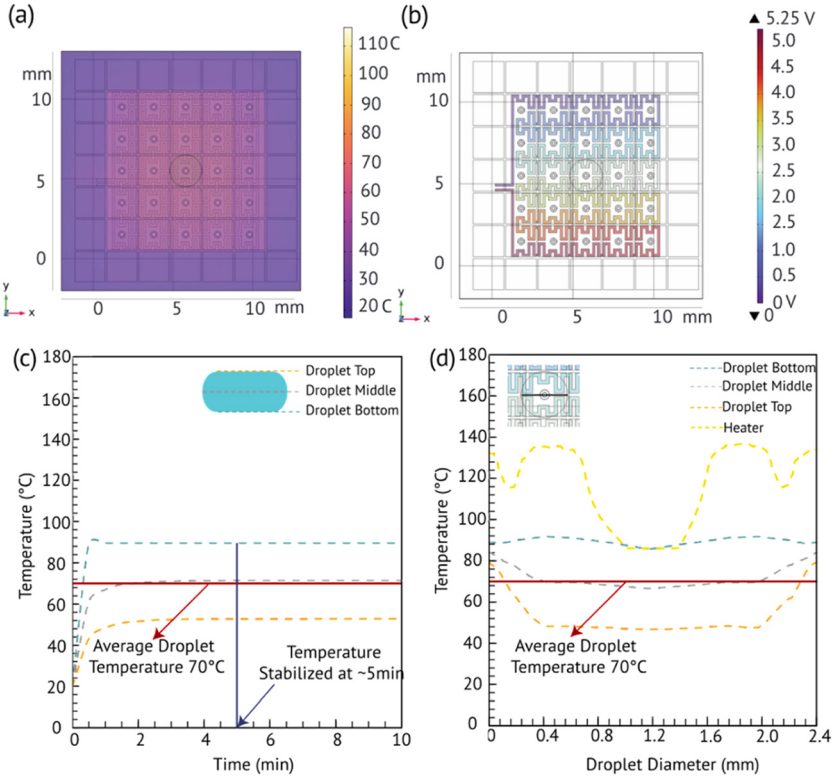

Fig. 2 The numerical simulation results illustrate the temperature distribution across the EWOD surface of the PCB, encompassing the thermal distribution of the droplet as well as the heater surface in a 2D view (a) under an applied voltage of 5.25 V at the heater terminals, colour legend shows the temperature in °C. Consequently, the voltage maps of the heater reveal a voltage gradient across the resistive heater (b). The voltage map confirms the serpentine-shaped heater which conducted across the PCB stack as well as the EWOD surface and droplet. The temperature stabilization over time demonstrates that the EWOD surface transitions from room temperature (20 °C) to a stable average temperature of 70 °C within ~5 minutes of applying voltage. At an applied voltage of 5.25 V, the droplet's bottom, middle, and top surface show temperature differences; however, the temperatures at these three levels stabilize within ~5 minutes, leading to an average droplet temperature of ~70 °C (c). To further understand the temperature variation within the droplet and heater at 5 min mark, a temperature plot has been developed (d). This plot specifically demonstrates the temperature variation along the diameter of the droplet as well as within the droplet, such as at the bottom, middle, and the top surface of the droplet as well as the temperature variation along the heater. The results indicate that the heater exhibits the highest temperature with variation due to the variation of the coil intensity as well as containing *via* (as shown in the inset), while the average droplet temperature reaches ~70 °C.

signal, the current supplied to the heater can be precisely controlled in the open-loop configuration. Programmatically, the PWM value, which typically ranges from 0–255 in an 8-bit microcontroller, regulates the power delivered to the heater, thereby controlling the generated heat. By adjusting the PWM signal's duty cycle, the power delivered to the resistor was precisely controlled. A longer duty cycle results in increased power and, consequently, greater heat generation by the resistor (Fig. S5(a)†).

Closed-loop controller design

An open loop generates outputs depending on the input variables, but external parameters may also affect the outputs. Maintaining a desired steady-state error and response time is difficult with an open loop. Therefore, a PID controller is utilized as a closed-loop feedback controller to obtain a consistent output from the device and decrease the influence of external disturbances. A PID controller maintains a stable temperature in a heater by dynamically adjusting the power input on the basis of the proportional, integral, and derivative terms of the temperature error, reducing overshoot, obtaining response time, and steady-state error. Therefore, to increase the accuracy and response time of the system, a closed-loop control mechanism using a PID controller was implemented (Fig. 3(c)). This configuration continuously monitors the temperature *via* the sensing circuit and adjusts the heater's power output to minimize the difference between the current temperature and the desired setpoint.

Through trial and error, the PID parameters (K_p, K_i, and K_d) can be manually tuned to achieve an optimal balance between rapid temperature response and minimal overshoot. However, in applications where manual tuning is not favorable, we also developed automatic PID tuning. Furthermore, to dynamically optimize the PID parameters, an automatic tuning algorithm was implemented. This feature continuously recalibrates PID parameters in real time,

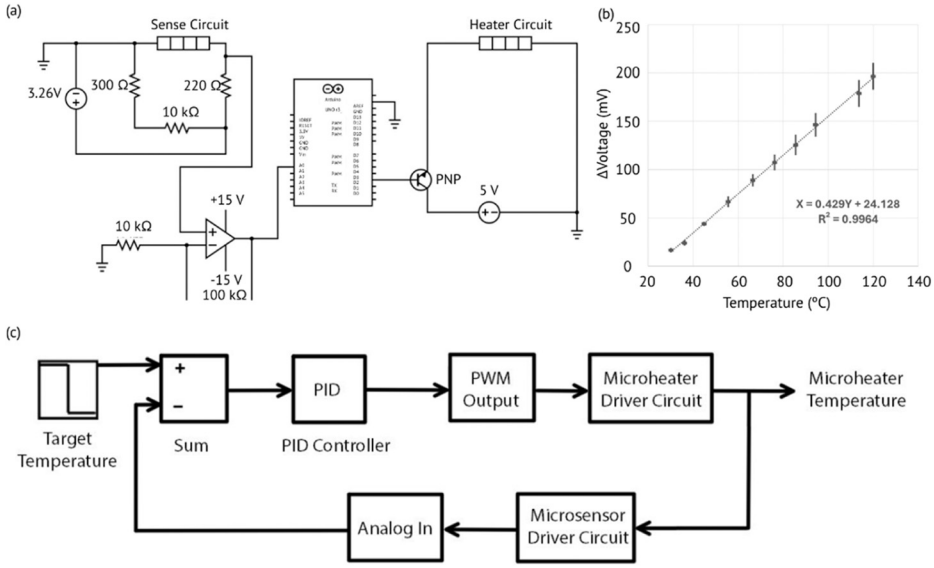

Fig. 3 Heating-sensing controller system consisting of (a) micro-sensor resistive temperature detection circuit in bridge configuration with one step amplification and PWM heater circuit, (b) calibration curve of the micro-sensor, and (c) closed-loop control with PID controller in the sense circuit. The sensor calibration curve shows a linear regression fit between the applied voltage and the corresponding output temperature of the sensor.

ensuring efficient system adaptation to dynamic conditions without manual intervention. Automatic tuning recalculates PID gains at predefined intervals, allowing the system to maintain optimal performance in dynamic environments while minimizing operator involvement.

On-chip glucose assay design

The objective of this experiment was to evaluate the applicability of an integrated heater and sensor for bioassay applications. For example, a standard glucose assay, traditionally known as Fehling's test, was developed and tested. The purpose of the glucose assay was to semiquantitatively detect the presence of reducing concentrations of sugars. For the purpose of this test, a commercially available glucose solution was used. Additionally, this test utilized Fehling's solution, a blue solution resulting from the presence of alkaline cupric hydroxide.[49]

The assay involved mixing a droplet of Fehling's solution with a droplet of diluted sugar solution at room temperature and heating the mixture to approximately 70 °C. The decrease in the concentration of sugars was indicated by a colour change in the solution, from blue to brownish-red, caused by the formation of cuprous oxide (Cu_2O) at elevated temperatures.

The test setup for performing the glucose assay on the *eDroplets* platform, which is designed to evaluate the functionality of the heating and sensing circuits in heating aqueous droplets, is illustrated in Fig. S6.† The setup also includes an image acquisition process to capture and analyze the colour transition of the droplets under the desired temperature conditions.

Results & discussion

Numerical simulation results

Fig. 2(a) depicts the temperature distribution across the EWOD surface of the PCB under an applied voltage of 5.25 V, showing a temperature range from 20 °C to 115 °C. Fig. 2(b) presents the voltage map of the heater under the same applied potential difference, illustrating its direct impact on the EWOD surface temperature profile. Fig. 2(c and d) shows the key simulation results, showing heat transfer from the integrated heater of the DMF chip to the droplet. The simulated voltage distribution of the microheater was analyzed, with a voltage of 5.25 V applied across the heater terminals to achieve an average droplet temperature of 70 °C at the droplet–electrode interface within an oil medium (Fig. 2(d)). The analysis highlights the temperature distribution across key components, including the microheater, the fluid–solid interface (droplet bottom and top), and the fluid–fluid interface (droplet middle). It also examines the time required for the droplet to stabilize at the target temperature (Fig. 2(c)) considering the possible delay shown in Fig. S7.†

To understand the time required to stabilize the temperature across the droplet, a time-dependent study was performed. According to the results, the temperature within the droplet, such as at the bottom of the droplet, within the droplet (such as the middle of the droplet), and at the top surface of the droplet, varies. However, the temperature stabilized within ~5 min (Fig. 2(c)). Furthermore, the average temperature within the droplet becomes ~70 °C.

To understand the temperature difference between the droplet and the microheater at ~5 min of heat generation, another temperature profile was used, as shown in Fig. 2(d). The heater temperature profile reveals that regions with higher

heater coil density exhibit elevated temperatures, which gradually decrease and stabilize near the vias on the PCB. Since the vias are filled with epoxy resin, they do not conduct significant heat, and there are no heater coils in close proximity to these regions. Consequently, the temperature profile plateaus before gradually rising and stabilizing at higher temperatures where the heater coil density increases. The temperature profile within the droplet shows a similar trend, as shown in Fig. 2(c), with an average temperature of 70 °C. Fig. 2(d) shows the temperature profile of the droplet at the droplet's bottom, middle, and top surfaces, as well as the heater. The temperature profile was taken along the diameter of the droplet, as indicated in the inset of Fig. 2(d). The temperature distribution profile across the planar surface, comparing experiments and simulations with and without a droplet, is shown in Fig. S8.† The simulated temperature distribution within the droplet along the vertical direction is presented in Fig. S9.†

Additionally, the simulation results reveal that the heat generated by the integrated heater is localized around its immediate vicinity and does not significantly conduct laterally across the PCB. This localized heating prevents thermal inertia within the system, regardless of the surrounding medium, thereby maintaining the efficiency and precision of the heating process.

Temperature sensor calibration

To measure the temperature of the heater using the inner microresistive sensor, proper signal conditions and calibration are needed. The resistance of the sensor works *via* a linear change in resistance with temperature, which can be related to the voltage drop across it. However, a bridge circuit is crucial for accurately measuring small resistance changes. Balancing the bridge enhances measurement precision by maximizing the voltage output corresponding to resistance variations. A bridge configuration is developed, as a resistive sensor responds to temperature changes, such as direct voltage measurements or simple voltage dividers, as shown in Fig. 3(a), which improves signal detectability, enabling precise temperature monitoring. To evaluate the ability of the integrated DMF chip to heat aqueous droplets *via* the integrated microheater and to assess the sensor's ability to accurately determine droplet temperature, a surface temperature calibration approach was then employed. This process also tested the functionality of both the sensing and heating circuits. During the calibration of the thin-film sensor, the applied voltage was recorded, and the corresponding surface temperature was measured *via* an attached precision thermocouple. The resulting data points were plotted with the change in voltage (ΔV) on the *X*-axis and the temperature on the *Y*-axis (Fig. 3(b)). By fitting a linear regression line to these data, we derived the following equation to relate the voltage change to the temperature for our sensor:

$$\text{Temperature} = 0.429(\Delta V) + 24.128$$

This linear relationship allows us to estimate the surface temperature based on the amplified voltage readings from the sensing circuit. This equation has an R^2 value of 0.9964, which indicates a strong linear relationship between the two variables. The accuracy of this equation and the sensing circuit setup ensures that the temperature of the surface can be measured using an integrated sensor layer reliably, without the need to use an external temperature probe and fulfill the original design goals for an integrated heating-sensing module for DMF.

Closed-loop temperature control

To achieve stability and accuracy of target temperature closed-loop control is necessary. For this purpose, we used a PID controller to regulate the microheater temperature by continuously adjusting the PWM signal based on real-time feedback from the temperature sensor described previously. The closed-loop control system with PID and PWM is shown in Fig. 3(c), which was implemented to ensure precise thermal control. This system is crucial as it minimizes temperature fluctuations, enhances stability, and improves efficiency by automatically correcting deviations from the desired setpoint. To further increase stability in real-time and to have minimal influence by external disturbances and dynamic tuning, the adaptive PID (APID) controller is then implemented, which provides further stability. Adaptive PID can dynamically adjust PID controller parameters in real time to optimize control performance and stability by responding to system variations and external disturbances. As shown in Fig. 4(a), we employed APID to maintain the temperature at 50 °C, 60 °C, 90 °C, and 95 °C. Apart from the stability of temperatures in the microheaters, often arrays of microheaters need to operate at different temperatures, where reducing unwanted heat transfer between the heaters is important for their performance and reliability. In many biochemical reactions, different thermal cycles with different temperatures may need to be run on a single chip, where thermal crosstalk can influence the performance of microheaters. Therefore, characterizing thermal crosstalk between adjacent, integrated and independent microheaters operating at different temperatures on the DMF chip is crucial for ensuring accurate and independent temperature control. The thermal images of the two adjacent heaters (B1 & B2) that were heated to various temperatures that are displayed in Fig. 4(b). Fig. 4(c) shows the heating profile over time, showing steady-state temperature stability between adjacent heaters without crosstalk. Fig. 4(d) shows the temperature distribution along the midline of the heat surface map having two adjacent heaters kept at 37 °C and 95 °C without cross-talk which will be useful for PCR applications.

Experimental results of the glucose assay and validation

To assess the capability and functionality of the new EWOD chip integrated with a heater and sensor and connected to

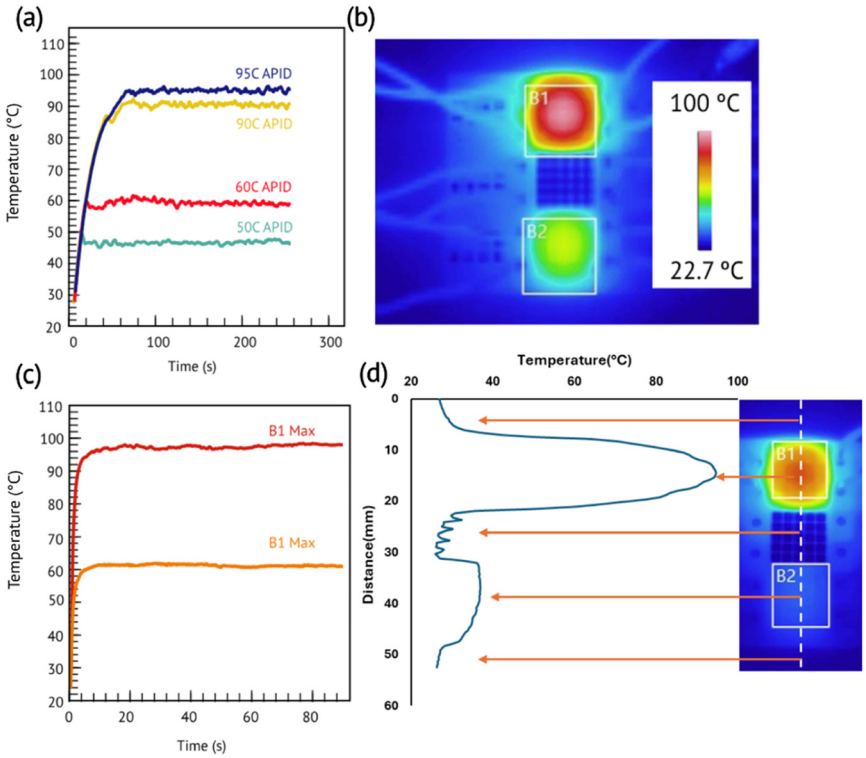

Fig. 4 Heater temperature control with the aid of APID controller. (a) The heater temperature stabilization over time with APID set at 50 °C, 60 °C, 90 °C, and 95 °C, (b) two adjacent heaters heating at different temperatures, (c) the temperature stabilization of the two adjacent heaters, (d) the temperature distribution along the line containing two heaters at different temperature at 37 °C and 95 °C.

the closed-loop controller, the glucose assay with Fehling's solution was performed. The Fehling's and glucose solution droplets were placed on the EWOD electrodes, and their movement was controlled to enable cohesive mixing, as shown in Fig. 5(a–c). The droplets were subsequently moved around to ensure uniform mixing, as illustrated in Fig. 5(d).

Once the two types of droplets were mixed, the merged droplet was positioned over the heater region, as depicted in Fig. 5(e). Before droplet placement on the heater, the heater was preheated to the target temperature to avoid the formation of microbubbles. The controller maintained the heater temperature at 70 °C, causing the color of the

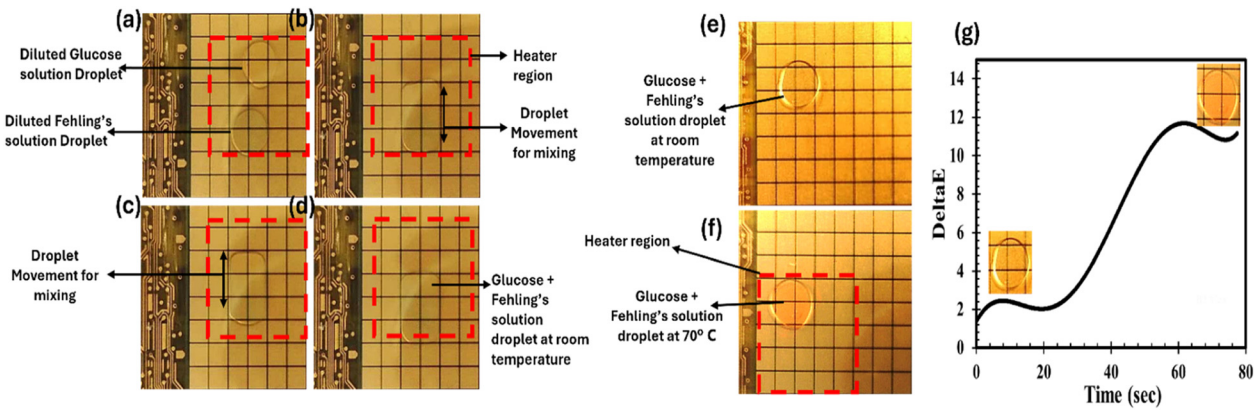

Fig. 5 To perform the glucose assay, Fehling's solution and glucose solution droplets were positioned on the EWOD surface of the *eDroplet* platform (a). The droplets were subsequently moved to merge and mix using the *eDroplets* DMF control system and GUI (b and c) and were positioned in the region containing the embedded microheater (d). These sequential steps allowed to mix the droplet to be heated to 70 °C for further analysis. Fehling's solution droplet and the glucose solution droplet were merged on the EWOD surface at the location of the embedded microheater. Initially, the merged droplet exhibited a light blue color (e), which transitioned to a brownish-red hue, indicating a heat-induced color change at 70 °C (f). A quantitative analysis revealed a gradual shift in the RGB values of the droplet from light blue to brownish-red, as determined using the DeltaE function over time. This colorimetric transition stabilized within 58 seconds, correlating with the stabilization of the surface temperature at 70 °C within the same timeframe (g).

droplet to change from light blue to brownish red because of the formation of cuprous oxide, as shown in Fig. 5(f). The experiment was recorded, and video frames were analyzed using MATLAB. RGB values were extracted and converted to scalar values using the DeltaE function. The function DeltaE depicts the color brightness and its location on the color scale by converting the three-dimensional axis color values into scalar values. The color change can then be compared to its initial position using this scalar value. A polynomial fit of the DeltaE values against time yielded an *R*-squared value of 0.9524, indicating a strong correlation. The DeltaE value began increasing at 24 s, stabilized at approximately 58 s, and confirmed the presence of reducing sugars in the solution (Fig. 5(g)). The stabilization timeframe of the DeltaE values correlates with the results of the numerical simulation, which also indicates that the EWOD surface temperature reached 70 °C within the same period. These results demonstrate the full functionality of the Arduino-operated PWM thermal controller to induce heat to the integrated microheater to efficiently transfer heat to the EWOD surface and subsequently to the solution droplet. They also validated the ability of the microcontroller to regulate the thermal response within minutes and accurately determine the temperature. This evidence highlights the efficiency of the microheater-integrated EWOD chip in performing heat-mediated chemical assays and underscores its potential applicability in advanced biochemical assays.

Conclusions

This paper presents the development of an integrated microheater and sensor for a novel DMF chip capable of generating localized heat and transferring it effectively from the microheater to an aqueous droplet within an oil or air medium on the EWOD surface. The heating, sensing, and EWOD elements are co-fabricated and compatible with commercial PCB manufacturing.

Experimental demonstration and validation of the heating platform, using a glucose assay demonstrated its reliability in performing assays and achieving the desired temperature and outcomes for DMF devices. This further highlights the effectiveness of the closed-loop, adaptive PID-based microcontroller designed for the microheater-integrated DMF chip. It precisely regulates the voltage applied to the microheater in real time, ensuring accurate surface temperature control and enhancing confidence in the system's performance.

The findings of this research support the execution of DMF operations without the need for external thermal components in DMF. Additionally, the entire system is cloud-based and commercially manufacturable by PCB manufacturers, making it accessible to users. This approach streamlines design, packaging, and device development, ultimately accelerating the adoption of the DMF platform in various lab-on-a-chip applications.

Data availability

Data supporting this article, including experimental and simulation results as well as related analysis and sources of materials and software are provided within the manuscript and in the ESI† file.

Author contributions

Conceptualization: M. J. A., C.-J. K., M. C., E. H. C., and Q. L. W. Investigation: M. C., G. N., E. H. C., Q. L. W., B., L. R., and A. A. Methodology: M. C., G. N., B., A. A., L. R., S. R. G., and C.-J. K. Project administration: M. J. A. and C.-J. K. Resources: M. J. A., S. R. G. and C.-J. K. Funding acquisition: M. J. A. and C.-J. K. Software: M. C., G. N., M. J. A., and C.-J. K. Writing – original draft: M. C., G. N., E. H. C., Q. L. W., B., A. A., M. J. A., and C.-J. K. Writing – review & editing: E. H. C., Q. L. W., S. R. G., M. J. A., and C.-J. K.

Conflicts of interest

There are no conflicts to declare.

Acknowledgements

MJA would like to thank the Natural Sciences and Engineering Research Council of Canada (NSERC) Alliance International Catalyst Grant (ALLRP 587354 – 23) for financial support. We thank CMC (Canadian Microelectronic Corporation) for CAD tools and equipment support. S. R.-G. thanks the Natural Sciences and Engineering Research Council of Canada (NSERC) for financial support through a Discovery Grant (RGPIN-2022-04428). C.-J. Kim would like to thank the National Science Foundation (1711708 and 1720499).

References

1 S. K. Cho, S. K. Fan, H. Moon and C. J. Kim, *Fifteenth IEEE International Conference on Micro Electro Mechanical Systems (MEMS)*, Las Vegas, NV, USA, 2002, Jan 20, pp. 32–35.
2 R. B. Fair, *Microfluid. Nanofluid.*, 2007, **3**, 245–281.
3 V. Srinivasan, V. K. Pamula and R. B. Fair, *Lab Chip*, 2004, **4**, 310–315.
4 M. G. Pollack, R. B. Fair and A. D. Shenderov, *Appl. Phys. Lett.*, 2000, **77**, 1725–1726.
5 S. K. Cho, H. Moon and C. J. Kim, *J. Microelectromech. Syst.*, 2003, **12**, 70–80.
6 J. Lee, H. Moon, J. Fowler, T. Schoellhammer and C. J. Kim, *Sens. Actuators, A*, 2002, **95**, 259–268.
7 H. Moon, S. K. Cho, R. L. Garrell and C. J. Kim, *J. Appl. Phys.*, 2002, **92**, 4080–4087.
8 X. Liu, D. Ma, H. Ye, Y. Hou, X. Bai, Y. Xing, X. Cheng, B. Lin and Y. Lu, *TrAC, Trends Anal. Chem.*, 2023, 117153.
9 H. Wang, L. Chen and L. Sun, *Front. Mech. Eng.*, 2017, **12**, 510–525.
10 K. Choi, A. H. C. Ng, R. Fobel and A. R. Wheeler, *Annu. Rev. Anal. Chem.*, 2012, **5**, 413–440.

11 A. Salari, J. G. C. Valenzuela, N. Le, J. Dahmer, A. A. Sklavounos, C. W. Kan, R. Manning, D. C. Duffy, N. R. Pollock and A. R. Wheeler, *Lab Chip*, 2025, **25**(7), 1669–1680.
12 Y. Chen, X. Wang, X. Na, Y. Zhang, L. Cai, J. Song and C. Yang, *Anal. Chem.*, 2024, **96**(31), 12916–12926.
13 T. Narahari, J. Dahmer, A. Sklavounos, T. Kim, M. Satkauskas, I. Clotea, M. Ho, J. Lamanna, C. Dixon, D. G. Rackus, S. J. R. d. Silva, L. Pena, K. Pardee and A. R. Wheeler, *Lab Chip*, 2022, **22**(9), 1748–1763.
14 M. Ho, N. Satishkumar, A. A. Sklavounos, J. Sun, I. Yang, K. P. Nichols and A. R. Wheeler, *Lab Chip*, 2024, **24**(1), 63–73.
15 B. J. Choelho, J. P. Neto, B. Sieira, A. T. Moura, E. Fortunato, R. Martins, P. V. Baptista, G. Igreja and H. Aguas, *Sensors*, 2023, **23**(10), 4927.
16 C. Yang, X. Gan, Y. Zeng, Z. Xu, L. Xu, C. Hu, H. Ma, B. Chai, S. Hu and Y. Chai, *Biosens. Bioelectron.*, 2023, **242**, 115723.
17 P. Y. Keng, S. Chen, H. Ding, S. Sadeghi, G. J. Shah, A. Dooraghi, M. E. Phelps, N. Satyamurthy, A. F. Chatziioannou, C. J. Kim and R. M. v. Dam, *Proc. Natl. Acad. Sci. U. S. A.*, 2012, **109**(3), 690–695.
18 R. Shen, A. m. Lv, S. Yi, P. Wang, P. I. Mak, R. P. Martins and Y. Jia, *TrAC, Trends Anal. Chem.*, 2023, **158**, 116826.
19 L. Wan, M. Li, M. K. Law, P. I. Mak, R. P. Martins and Y. Jia, *Biosens. Bioelectron.*, 2023, **242**, 115711.
20 T. Chen, Y. Jia, C. Dong, J. Gao, P. I. Mak and R. P. Martins, *Lab Chip*, 2016, **16**(4), 743–752.
21 Y.-H. Chang, G.-B. Lee, F.-C. Huang, Y.-Y. Chen and J.-L. Lin, *Biomed. Microdevices*, 2006, **8**, 215–225.
22 W. C. Nelson, I. Peng, G. A. Lee, J. A. Loo, R. L. Garrell and C. J. Kim, *Anal. Chem.*, 2010, **82**, 9932–9937.
23 K. Ugsornrat, N. V. Afzulpurkar, A. Wisitsoraat and A. Tuantranont, *Sens. Mater.*, 2010, **22**(6), 271–284.
24 T. Hoang, B. H. Ly, T. X. Le, T. T. Huynh, H.-T. Nguyen, T. V. Vo, T. T. H. Pham and K. Huynh, *Microsyst. Technol.*, 2020, **26**, 1863–1873.
25 J. Shen, L. Zhang, J. Yuan, Y. Zhu, H. Cheng, Y. Zeng, J. Wang, X. You, C. Yang, X. Qu and H. Chen, *Anal. Chem.*, 2021, **93**(45), 15033–15041.
26 M. Li, L. Wan, M.-k. Law, L. Meng, Y. Jia, P. I. Mak and R. P. Martins, *Lab Chip*, 2022, **22**(3), 537–549.
27 K.-L. Ho, H.-Y. Liao, H. M. Liu, Y.-W. Lu, P.-K. Yeh, J. Y. Chang and S.-K. Fan, *Micromachines*, 2022, **13**(2), 196.
28 P. C. Gach, S. C. C. Shih, J. Sustarich, J. D. Keasling, N. J. Hillson, P. D. Adams and A. K. Singh, *ACS Synth. Biol.*, 2016, **5**(5), 426–433.
29 E. Moazami, J. M. Perry, G. Soffer, M. C. Husser and S. C. C. Shih, *Anal. Chem.*, 2019, **91**(8), 5159–5168.
30 J. M. Perry, G. Soffer, R. Jain and S. C. C. Shih, *Lab Chip*, 2021, **21**(19), 3730–3741.
31 D. Millington, S. Norton, R. Singh, R. Sista, V. Srinivasan and V. K. Pamula, *Expert Rev. Mol. Diagn.*, 2018, **18**(8), 701–712.
32 M. Alistar and U. Gaudenz, *Bioengineering*, 2007, **4**, 45.
33 R. Fobel, C. Fobel and A. R. Wheeler, *Appl. Phys. Lett.*, 2013, **102**(19), 193513.
34 A. Stephenson, M. Wilsey, J. McBride, S. Newman, B. Nguyen, C. Takahashi, K. Strauss and L. Ceze, *IEEE Micro*, 2020, **40**(5), 76–86.
35 L. Wan, J. Gao, T. Chen, C. Dong, H. Li, Y.-Z. Wen, Z. R. Lun, Y. Jia, P. I. Mak and R. P. Martins, *Biomed. Microdevices*, 2019, **21**, 1–8.
36 D. Albin, L. Buecherl, E. Kochavi, E. Niehaus, S. Novack, S. Uragoda, C. J. Myers and M. Alistar, *IEEE Trans. Biomed. Eng.*, 2023, **71**(1), 217–226.
37 T. Kremers, S. Thelen, N. Bosbach and U. Schnakenberg, *PLoS One*, 2020, **15**(9), e0238581.
38 S. Anderson, B. Hadwen and C. Brown, *Lab Chip*, 2021, **21**(5), 962–975.
39 J. Gong and C. J. Kim, in *Proc. of 18th IEEE International Conference on Micro Electro Mechanical Systems (MEMS)*, 2005, Jan 30, Miami Beach, USA, pp. 726–729.
40 P. Y. Paik, V. K. Pamula, M. G. Pollack and K. Chakrabarty, *MicroTAS*, 2005, Oct 9, Boston, Massachusetts, USA, pp. 566–568.
41 J. Li and C. J. Kim, *Lab Chip*, 2020, **20**, 1705–1712.
42 C. Zhang and D. Xing, *Nucleic Acids Res.*, 2007, **35**(13), 4223–4237.
43 D. Seehase, A. Neiser, F. Lange, A. Novikov and M. Nowottnick, in *2018 7th Electronic System-Integration Technology Conference (ESTC)*, 2018, Sep 18, Dresden, Germany, pp. 1–9.
44 D. Wu, R. Ng, G. Smith, V. Srinivasan and V. Pamula, WO2022/256514A1, 2022.
45 G. Tanev, W. S. S. Svendsen and J. Madsen, *Micromachines*, 2022, **13**, 249.
46 G. White, US9012811B2, 2015.
47 Q. L. Wang, E. H. Cho, J. Li, H.-C. Huang, S. Kin, Y. Piao, L. Xu, K. Tang, S. Kuiry, Z. He, D. Yu, B. Cheng, C.-C. Wu, C. Choi, K. Shin, T.-Y. Ho and C.-J. Kim, *Lab Chip*, 2024, **24**(19), 4536–4548.
48 Q. L. Wang, J. Li, H.-S. E. Cho, L. Xu, A. Wang, S. Kuiry, Z. He, J. Ho and C. J. Kim, in *2024 IEEE 37th International Conference on Micro Electro Mechanical Systems (MEMS)*, 2024, Jan 21, Austin, TX, USA, pp. 1138–1141.
49 G. J. Gerwig, *The Art of Carbohydrate Analysis, in Techniques in Life Science and Biomedicine for the Non-Expert*, Springer International Publishing, Cham, 2021, DOI: **10.1007/978-3-030-77791-3**.